國 立 交 通 大 學

電 子 工 程 學 系 電 子 研 究 所

碩 士 論 文

奈米尺寸金氧半場效電晶體通道背向散射：蒙地卡羅模擬與物理模型

Nanoscale MOSFETs Channel Backscattering: Monte Carlo Simulation and Physical Model

研 究 生：呂立方　　Li-Fang Lu

指導教授：陳明哲　　Prof. Ming-Jer Chen

中華民國　九十七　年　七　月

奈米尺寸金氧半場效電晶體通道背向散射:

蒙地卡羅模擬與物理模型

Nanoscale MOSFETs Channel Backscattering:

Monte Carlo Simulation and Physical Model

研 究 生：呂立方　　Student：Li-Fang Lu

指導教授：陳明哲　　Advisor：Prof. Ming-Jer Chen

國 立 交 通 大 學

電子工程學系 電子研究所碩士班

碩 士 論 文

A Thesis

Submitted to Department of Electronics Engineering &

Institute of Electronics

College of Electrical and Computer Engineering

National Chiao Tung University

in Partial Fulfillment of the Requirements

for the Degree of

Master of Science

In

Electronics Engineering

July 2008

Hsinchu, Taiwan, Republic of China

中華民國　九十七　年　七　月

奈米尺寸金氧半場效電晶體通道背向散射:
蒙地卡羅模擬與物理模型

研究生：呂立方　　指導教授：陳明哲博士

國立交通大學

電子工程學系電子研究所

摘　要

藉由散射矩陣的方法，可以推導出背向散射係數，再利用蒙地卡羅模擬証明。組成背向散射係數的兩個重要的參數—λ_0和ℓ—也在論文中有進一步地討論；ℓ的物理解析式模型建立在源極到通道上假設的拋物線能障上，也藉由實驗以及蒙地卡羅模擬得到驗證。藉由蒙地卡羅模擬得到在入射處的速度分佈推斷平均自由路徑的縮短源自於載子熱效應，然而在拋物線能障的情況下因為沒有熱載子效應，使得平均自由路徑維持定值。

Nanoscale MOSFETs Channel Backscattering: Monte Carlo Simulation and Physical Model

Student：Li-Fang Lu Advisor：Prof. Ming-Jer Chen

Department of Electronics Engineering

Institute of Electronics

National Chiao Tung University

Abstract

Through the scattering matrix approach, the backscattering coefficient is derived and it is verified by Monte Carlo simulations. Two important parameters, λ_0 and ℓ, constituting the channel backscattering have been taken into account. A parabolic barrier oriented compact model has been physically derived for ℓ. The validity of this compact model has been corroborated experimentally and by Monte Carlo simulation results. As for λ_0, the carrier heating as the origin of reduced mean-free-path is inferred on the basis of the simulated carrier velocity distribution at the injection point. Strikingly, for the parabolic potential case, the mean-free-paths remain consistent: $\lambda' = \lambda_o$. This indicates the absence or weakening of the carrier heating in the layer of interest, valid only for a parabolic potential barrier

致　謝

感謝陳明哲教授，在這兩年的教導之下，充分地感受與學習到老師對做學問的嚴謹態度，再加上跟老師不時的討論並指點我正確的方向，讓我得在做研究的路途上一步一步地順利完成每一個階段的任務。在此我要由衷地向老師表達我的感謝之意。

非常感謝博士班學長們給的許多指導和意見，謝振宇學長給予的專業方面的指點，李建志學長在體育方面的競技，許智育、李韋漢學長在休閒、課業方面的討論，以及實驗室碩二的同伴們的互相鼓勵。

這幾段話是沒辦法一一謝過所有關心我的人，故以此感言獻給每一位關心我的人，感謝你們，謝謝！

呂立方

Contents

List of Captions

Chapter 1

Introduction

The scaling down of silicon MOSFETs has promisingly moved from 180nm to 65nm node in the past decade. The ITRS also predicts that this scaling trend will reach 22nm technology node in the coming decade. This amazing evolution of silicon technology leads to challenges about how carriers transport in nanoscale devices, specially the losing efficiency of some classical-based carrier transport models such as drift-diffusion transport model. In the beginning of this promising decade, another aspect of carrier transport theory, named “Backscattering Theory”, was proposed by Mark Lundstrom [1]-[2]. This theory is different from drift-diffusion based model. Instead, current-voltage (I-V) characteristics are expressed in terms of the elementary parameters without depending on the carrier mobility. These parameters, such as carrier injection velocity and inversion carrier density at the virtual source, control the device performance. In other words, device performance can no longer be considered only by the channel itself.

In the Backscattering theory, we distinguish the carrier transport in the channel as a wave-like flux traveling from source to drain. According to the theory, the key region controls the flux ratio passing through the channel named ℓ, which is the distance over which the channel potential drops by $\frac{k_B T}{q}$ (k_B is the Boltzmann’s constant and T is the temperature). Multiple backscattering events occur in this critical zone. Thus, a certain fraction r_c of the injecting flux F is reflected and returns to the source, and the remaining flux (1-r_c)F transmits to the drain. Figure 1-1 demonstrates

scattering events and returning flux schematically. Backscattering theory relates the steady-state current to transmission and reflection coefficients. Consequently, the drain current per unit channel width, which is critically determined by ℓ, can be expressed as

$$I_D = Q_{inv} v_{inj} \frac{(1-r_c)}{(1+r_c)} \quad (1)$$

where Q_{inv} is the inversion-layer charge density per unit area at the top of the virtual source, v_{inj} is the thermal injection velocity at the top of the virtual source, and r_c is the channel backscattering coefficient through this critical layer. Backscattering theory also relates to both the near-equilibrium mean-free-path λ_0 (or called momentum relaxation length) and the critical length of the k_BT layer:

$$r_c = \frac{\ell}{\ell + \lambda_0} \quad (2)$$

Eq.(2) is valid only for drain voltage much larger than k_BT/q. Here, r_c can be extracted experimentally by current-voltage (I-V) fitting [3] or by a temperature dependent method [4]. The temperature dependencies of the k_BT layer's width also are clarified by methods of temperature oriented experiment and simulation [5]. However, these two important parameters in (2) must be discussed more clearly. First, expression of ℓ used in the open lecture is in lack of gate voltage effect, and, we usually assume ℓ as a function of lattice temperature, channel length and applied voltage (V_D). Besides, the temperature dependent power order of ℓ range from 0.5 to 1 [3]-[8]. Second, the usage of λ_0, called near-equilibrium mean-free-path for backscattering, must be clarified.

In this thesis, we present a new compact model for ℓ on the basis of a parabolic potential barrier profile assumption around the source-channel junction. This compact model is physically derived and can elucidate the effects of channel length, gate

overdrive, drain voltage and the temperature on ℓ. Additionally, 1-D Monte Carlo particle simulation [13] is performed to explore the backscattering coefficient r_c, which is related to the mean-free-path λ_0. Evidence about carrier heating can be found accordingly.

This thesis is organized as follows. In Chapter 2, we derive the backscattering coefficient through scattering matrix approach and Monte Carlo simulations are executed to verify the validity of the derivation. In Chapter 3, a parabolic barrier oriented compact model is physically derived and verified by experimental data and simulation results. In Chapter 4, another important parameter λ_0 is discussed. Finally, a conclusion of the work will be drawn in Chapter 5.

Chapter 2

Backscattering Coefficient

and Monte Carlo Simulation

In this chapter, the origin of the backscattering coefficient r_c, under both low applied voltage ($V_a << k_BT/q$) and high applied voltage ($V_a >> k_BT/q$) conditions, is derived using the scattering matrix approach [9]. Then, we will employ the existing particle-based Monte Carlo simulator to deal with the velocity distributions that are relevant to the desired backscattering coefficient r_c.

Section 2.1 Backscattering Coefficient

The underlying carrier transport from the top of the source-channel barrier, or called the virtual source, down to the drain contact can be treated using the scattering matrix approach [9]. However, there are some assumptions that must be introduced. First, we assume that the flux is only emitted from the virtual source; in other words, there is no flux emitted from the drain contact. Second, we assume that the flux traveling from the top of the virtual source down the potential drop is not affected by the electric field. Third, we assume steady-state conditions, which means right-directed flux **a(x)** and left-directed flux **b(x)** are position dependent, while being independent of time. The recombination-generation processes are also neglected. Under these assumptions, the change of the positive-directed flux ***a*** and negative-directed flux ***b*** due to the backscattering event over the ***dx*** path interval at the position ***x*** can be described as

$$\frac{db}{dx} = -\frac{a}{\lambda_0} + b\left(\frac{1}{\lambda_0} + \frac{q}{k_B T}\left|\varepsilon_\ell\right|\right) \tag{8}$$

where ε_ℓ is the electric field and λ_0 is the mean-free-path for backscattering. We know that the net flux ***a* – b**, as a result of the flux conservation through all sections, has to be kept constant. To solve (8) in the zone of interest where: $\left|\varepsilon_\ell\right| \approx \frac{k_B T}{q\ell}$ [1], we have

$$b(0) = \frac{1 - \exp(-\frac{x}{\ell})}{\frac{\lambda_0}{\ell} + 1 - \exp(-\frac{x}{\ell})} a(0) + \frac{1}{(1 + \frac{\ell}{\lambda_0})\exp(\frac{x}{\ell}) - \frac{\ell}{\lambda_0}} b(x) \tag{9}$$

From the second assumption, we can know that the left-directed flux **b** at the drain contact is equal to zero, ***b(L)=0***. Thus, the complete expression of the r_c can be written as

$$r_c = \frac{1 - \exp(-L/\ell)}{\frac{\lambda_0}{\ell} + 1 - \exp(-L/\ell)} \tag{10}$$

Apparently, for applied voltage $V_a >> k_B T/q$, also L>>ℓ, (10) reduces to (2). For $V_a << k_B T/q$ or L<<ℓ, opposite to the former case, (10) reduces to the near-equilibrium case prevailing over the entire channel [11]

$$r_c = \frac{L}{L + \lambda_0} \tag{11}$$

In the citation [1], reproduction of the simulation results in the transition region between the low and high field limits can be conducted via the product of (11) and (2), and is some what empirical. Here, (10) can be readily used for not only high V_a and low bias but also the transition region. In the citation [10], the same expression is solved from the Boltzmann transport equation in the framework of a “relaxation length” approximation.

Section 2.2 Monte Carlo Simulation

In order to verify (10), we adopt the Monte Carlo simulation. This particle-based Monte Carlo technique is recognized as a powerful method for accurately describing the carrier transport in semiconductor materials and devices within the semi-classical approximation. Here, we use Monte Carlo simulation program to solve the complicated scattering events in a silicon bulk conductor. This program named Demons [13] can provide the rich information regarding the carrier velocity distributions at any positions in the conductor. Furthermore, the positively-directed flux and the negatively-directed flux can be separately determined, which means the flux ratio at any position can be easily obtained.

Section 2.2.1 Simulation Methodology

Before performing Monte Carlo simulation, some assumptions and boundary conditions must be clarified: (i) carriers are only injected one by one at the origin **x=0** in the steady state from the left contact and are of hemi-Maxwellian distribution; (ii) termination condition: at the origin **x=0**, left contact absorbs backscattered carriers without further reflections, and at the end of the conductor, **x=L**, the positively-directed carriers are absorbed; (iii) the potential profile in the conductor is not self-consistent but frozen, just like other group adopted [10],[12]; and (iv) the conductor is divided into 100 grids, as shown in Fig.2-1, to analyze the positive-directed flux and negatively-directed flux in each grid. Figure 2-1 schematically depicts this simulation picture.

In this work, we perform Monte Carlo simulation at three different lattice temperatures, (150, 200 and 300 K), four different conductor lengths, (15, 25, 50 and 100 nm). Moreover, these simulations are executed in two potential profile cases: linear and parabolic potential, which are displayed in Fig.2-2. In our group previous work [5], linear potential profile case has been performed on 80-nm silicon conductor

of 10^{12} cm^{-3} doping to examine the temperature dependencies of the width spanned by ℓ. However, parabolic potential case is the significant augmentation. It has been experimentally shown to be a good approximation to build near –source channel conduction-band profile of MOSFET in saturation [7]. Besides, by using the basis of parabolic potential profile around the source-channel junction barrier of nanoscale MOSFETs, a compact new model of k_BT-layer width is physically derived [14]. We will discuss this compact model in the subsequent chapter.

Section 2.2.2 Determination of r_c

From the definition of backscattering coefficient, we have

$$r_C = \frac{flux(-)}{flux(+)} = \frac{n^- v^-}{n^+ v^+} \tag{12}$$

where $\dfrac{v^-}{v^+} = \dfrac{\dfrac{\int_{-\infty}^{0} f(v) v dv}{\int_{-\infty}^{0} f(v) dv}}{\dfrac{\int_{0}^{\infty} f(v) v dv}{\int_{0}^{\infty} f(v) dv}}$,

and $\dfrac{n^-}{n^+} = \dfrac{\int_{-\infty}^{0} f(v) dv}{\int_{0}^{\infty} f(v) dv}$.

$n^{\pm}$ is the electron density for positively-directed / negatively-directed flux on the top of the barrier, and $v^{\pm}$ is the average velocity for positively-directed and negatively-directed flux on the top of the barrier. Figure 2-3 shows the simulated velocity distribution of conductor length 100 nm with 10^{12} cm^{-3} doping, 300K temperature and 0.6 V applied voltage in linear potential case at the **x=0**. Here, the backscattering coefficient r_c is just equal to the area ratio of deep gray one to light gray one. Likewise, we can see that the injected carriers still retains hemi-Maxwellian distribution but is split into two distinct components: one of the longitudinal effective

mass and one of the transverse effective mass.

Section 2.2.3 Mean-Free-Path for Backscattering

If we want to use (10) to evaluate the simulation r_c data, we need information for two important parameters: mean-free-path for backscattering λ_0 and corresponding k_BT-layer's width ℓ. However, according to the backscattering framework [1-2], ℓ can be explicitly expressed as a function of the thermal energy k_BT, the conductor length L, and the applied voltage V_a. For this reason, we have $\ell = L\frac{k_BT}{qV_a}$ for the linear potential profile and $\ell = L\sqrt{\frac{k_BT}{qV_a}}$ for the parabolic one.

Since the k_BT-layer's width is clearly defined, in order for calculations from (10) to have good agreement with simulated r_c, mean-free-path for backscattering λ_0 should be obtained accurately. We can extract λ_0 via (11) on the longest conductor (L = 100 nm) in the low electric filed, $V_a << k_BT/q$, that is to say, $L >> \ell$. Figure 2-4 shows the extracted results for three different temperatures of 150, 200 and 300 K. In the figure, the bar represents the range of simulated r_c values. The average r_c of a linear potential profile is close to that of the parabolic one, which indicates λ_0 is essentially independent of the potential profile we adopted in the low field regime. The average r_c over these two potential profiles leads to the average λ_0 of 56, 105, and 155 nm for 300, 200 and 150 K, respectively. The extracted average value of λ_0 at 300 K is identical to that of our group previous work [5].

Section 2.3 Result and Verification

Since the mean-free-path for backscattering is extracted via (11) in the low electric field or near-equilibrium condition. The corresponding ℓ is $\ell = L\frac{k_B T}{qV_a}$ for the linear potential profile and $\ell = L\sqrt{\frac{k_B T}{qV_a}}$ for the parabolic one. Figure 2-5 and 2-6 show the simulated r_c in symbols and (10) in dotted lines. Comparison between linear potential profile and parabolic one, it is easy to find out that there is discrepancy in the linear potential profile between calculations and simulation values. This deviation increases with decreasing conductor length and decreasing lattice temperature. However, Figure 2-6 shows good agreement between the simulated r_c and that of (10). In order to discuss this discrepancy, we have to investigate two important parameters, ℓ and λ_0, in (10). First, according to the open literature [1-2], when V_a is much larger than $k_B T/q$, the definitions of the k_BT-layer's width in both potential profiles have been defined. Second, the other parameter λ_0 is called near-equilibrium mean-free-path for backscattering. We extracted λ_0 via (11) in the low electric field or near-equilibrium condition, and it is the only mean-free-path used for all operating conditions. In [10], the similar expression of (10) is also derived via Boltzmann transport equation in the framework of a "relaxation length" approximation, and within that approximation, mean-free-path λ_0 must be independent of carrier energy. In other words, λ_0 has to be constant no matter how large the applied voltage is. However, Monte Carlo simulation results at room temperature in linear potential profile show that λ_0 should change. Certain relationship, $\lambda' = \lambda_0 / \gamma$ with γ=1.5 to 2.0, is discovered [15]. We will discuss this issue later.

Chapter 3

A Parabolic Barrier Oriented Compact Model for the k_BT Layer's Width

The channel backscattering theory [1-2] establishes a connection between the k_BT-layer's width, which locates in the beginning of the conductive channel near the source, and the drive performance of the device. However, the ability to quantitatively determine the width of this critical zone is necessary. We have discussed the backscattering coefficient through scattering matrix approach and performed Monte Carlo simulation in Chapter 2. Although ℓ can be explicitly expressed as a function of the conductor length L, the thermal energy k_BT, and the applied voltage V_a, this expression can not elucidate the effect of gate voltage on ℓ. Moreover, the influence of temperature on ℓ should be discussed more clearly. In this chapter, a parabolic potential barrier oriented compact model for k_BT-layer's width in nano-MOSFETs is derived, and will be verified by experiment and simulation.

Section 3.1 Discrepancy in Temperature Dependency

Mostly adopted model of ℓ can be quoted in the literature [6],

$$\ell = L(\frac{k_BT}{qV_a})^{\alpha} \tag{13}$$

where ℓ is the k_BT-layer's width and L is the conductor channel length. In the previous chapter, we can easily define ℓ in both linear and parabolic potential profile with $\alpha = 1$ and $\alpha = 0.5$, respectively. However, some division among the magnitude of the temperature exponent α should be clarified. In the first place, the I-V characteristics of a simulation double-gate MOSFET at room temperature can be

best fitted by $\alpha = 0.57$ [6]. In addition, comparable $\alpha = 0.5$ has been produced on experimental bulk n-MOSFETs in a temperature range of 233 to 298 K [5], [7]. Besides, $\alpha = 0.75$, which covers the same range as the former case, has been experimentally determined [3]. Still, $\alpha = 1$ has already been adopted in a temperature dependent backscattering coefficient extraction method [4]. Another open literature [8] also shows that ℓ is approximately proportional to the temperature form 100 to 500 K, which means $\alpha = 1$. Apparently, the issue of widely-ranged α values must be addressed. Furthermore, it is difficult for (13) to elucidate the effect of gate voltage. We will make a simple approach by assuming a parabolic potential near the source-channel junction. Then a compact model with the channel, gate overdrive, drain voltage, and temperature as input parameters will be physically derived.

Section 3.2 Parabolic Barrier Profile

A parabolic potential profile close to the source is schematically plotted in Figure 3-1. This potential profile that extends to the remaining channel can be described as

$$V(x) = V_D (x / \tilde{L})^2 \tag{14}$$

The origin x=0 is the peak of the barrier. $\tilde{L}$ indicates the imaginary channel length corresponding to a certain position where the parabolic potential drop from the top of the barrier is equal to V_D. At the other side, we neglect the barrier height with respect to the source side because of the large drain voltage. Then, by substituting $x = \ell$ and $V(x) = k_B T / q$ into (14), which means a local potential drop being equal to thermal energy, the ℓ expressed in terms of imaginary $\tilde{L}$, applied voltage V_D, and thermal energy $k_B T$ can be obtained:

$$\ell = \tilde{L}(\frac{k_B T}{qV_D})^{\frac{1}{2}} \tag{15}$$

Obviously, once $\tilde{L}$ can be expressed as a function of channel length, gate voltage, drain voltage and temperature, the expression of ℓ in terms of these parameters can be obtained.

There exists a set of specific drain voltage V_{D0} and gate voltage V_{G0}, at a given temperature T_0, which can ensure $\tilde{L} = L$:

$$\tilde{L}(T = T_0, V_D = V_{D0}, V_G = V_{G0}) = L \tag{16}$$

That is to say, this imaginary $\tilde{L}$ just locates on the real channel length. Then, we will discuss each component in later sections.

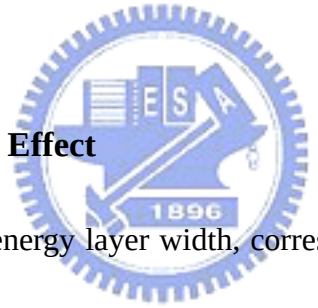

Section 3.2.1 Temperature Effect

First of all, the thermal energy layer width, corresponding to $\tilde{L} \to L$, $T \to T_0$, and $V_D \to V_{D0}$, is denoted as ℓ_0. ℓ_0 can be expressed as

$$\ell_0 = L(\frac{k_B T_0}{qV_{Do}})^{\frac{1}{2}} \tag{17}$$

Then only the temperature changes individually from T_0 to T. By dividing (15) by (17), a power-law relation can be found:

$$\tilde{L} = L(T/T_0)^{\frac{1}{2}} \tag{18}$$

Here, we have assumed that the potential profile does not change with temperature. In other words, the local electric field from the peak of the barrier to the end of k_BT-layer is approximately the same in these two temperatures. According to the backscattering

theory [1], the local electric fields across this section are equal to $k_B T_0 / q\ell_0$ and $k_B T / q\ell$ at T_0 and T, respectively.

Section 3.2.2 Gate Voltage Effect

Once the potential profile is assumed, we can easily differentiate (14) twice with respect to position x, which leads to

$$\frac{d^2V(x)}{dx^2} = \frac{2V_D}{\tilde{L}^2} \tag{19}$$

Under the same V_D, and according to Poisson's equation, (19) relates to the charge density. From [6], we can know that (19) also can be linearly related to the underlying inversion-layer density, which is proportional to the gate overdrive. It turns out that

$$\tilde{L} = L\left(\frac{(V_{G0} - V_{th})}{(V_G - V_{th})}\right)^{\frac{1}{2}} \tag{20}$$

Here, the term, $(V_{G0} - V_{th})$ represents the specific gate overdrive that ensures (16).

Section 3.2.3 Drain Voltage Effect

The local electric field can be obtained by differentiating (14) once. Thus, if the drain voltage increases from V_{D0} to V_D, local electric field, $\frac{2V_D x}{\tilde{L}^2}$, must be larger that $\frac{2V_{D0} x}{L^2}$. If the local electric fields were equal, we could know that $\tilde{L} = L(V_D / V_{D0})^{0.5}$. Because $V_D > V_{D0}$, the electric field is increased. Thus the power exponent must be no more than 0.5. As a result, one obtains

$$\tilde{L} = L(V_D / V_{D0})^{\nu=0.25} \tag{21}$$

The power exponent ν, which is equal to 0.25, has been experimentally determined in the previous work of our group [7]. For $V_D < V_{D0}$, the same expression as (21) can be obtained.

Section 3.2.4 Combination of Temperature and Bias Effects

Through the combination of (18), (20), and (21), these power-law relationships establish a unique expression for $\tilde{L}$:

$$\tilde{L} = \eta L \frac{V_D{}^{0.25}}{(V_G - V_{th})^{0.5}} \left(\frac{k_B T}{q} \right)^{0.5} \tag{22}$$

Combining (15) and (22) can further lead to

$$\ell = \eta L \frac{V_D{}^{0.25}}{(V_G - V_{th})^{0.5}} \left(\frac{k_B T}{q} \right)^{0.5} \left(\frac{k_B T}{q V_D} \right)^{0.5} \tag{23}$$

where $\eta = \frac{(V_{G0} - V_{th})^{0.5}}{V_{D0}{}^{0.25}} \left(\frac{k_B T_0}{q} \right)^{-0.5}$. Furthermore, η is fixed and also the only fitting parameter in this expression. Indeed, it is supposed that η is a constant value over the channel length, gate and drain voltage, and temperature. Thus, the capability of this parabolic potential barrier oriented compact model will be more general.

Section 3.3 Model Verification

On the one hand, the experimental ℓ in this section was obtained from 55-*nm* bulk n-MOSFETs by means of a parameter extraction process proposed by our group, and the details can be found in [3], [5], [7]. On the other hand, we quoted the rich literature [8],[19], in which Monte Carlo simulations including quantum corrections to the potential and calibrated scattering models are used to study carrier transport in bulk and double-gate silicon-on-insulator MOSFETs. Also cited are those of the open

literature [2], [6], [16], [17], [18].

Section 3.3.1 Experimental Validation

Figure 3-2 shows the experimental ℓ, which is obtained from 55-*nm* bulk n-MOSFETs with t_{ox}=1.65nm, N_{poly}=1x$10^{20}$$cm^{-3}$, and N_A=7x10^{17} cm^{-3}, versus gate voltage for two drain voltages of 0.5 and 1.0 V and three different temperatures of 233, 263, and 298 K. With these experimental ℓ values, temperature *T*, and applied drain voltage V_D, we can obtain the corresponding $\tilde{L}$ using (15). These results are shown in Figure 3-3 for two drain voltages versus gate voltage. The corresponding near-equilibrium threshold voltage, denoted V_{tho} for 233, 263, and 298K are 0.360, 0.345, and 0.328 V, respectively. The drain-induced barrier lowering (*DIBL*) magnitude for 233, 263, and 298K are 120, 123, and 130 mV/V, respectively. Throughout this work, the threshold voltage V_{th} at higher drain voltages is equal to $V_{tho} - DIBL \times V_D$.

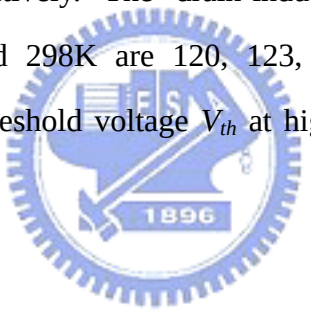

Section 3.3.2 Simulation Validation

First, in Ref. [8], the extracted ℓ at $V_D = V_G$ = 1 V is available in a wide range of the channel length from 14 to 37 nm and also a wide range of the temperature from 100 to 500 K. The underlying threshold voltage V_{tho} and *DIBL* are reasonably 0.3 V and 110 mV/V, respectively. Second, the citation [19] can further provide the relevant information at room temperature: ℓ from 2.0 to 7.0 nm, L from 14 to 65 nm, V_D (= V_G) from 1.0 to 1.2 V, and DIBL from 11 to 230mV/V. The above information is listed in Table 3-1. Moreover, we have also extracted ℓ from the published literature [6], [8], [16-18], on double-gate device simulation and ℓ can be extracted directly from the channel potential profiles. The corresponding key parameters are: (i) L = 10 nm, $V_{tho} \approx$ 0.33 V, *DIBL* ≈140 mV/V, V_D = 0.6 V, V_G = 0.6 V, and T = 300 K [2]; (ii) L = 20

nm, $V_{tho} \approx 0.33$ V, *DIBL* ≈ 25 mV/V, $V_D = 0.2$ V, $V_G = 0.55$ V, and $T = 300$ K [6]; (iii) $L = 25$ nm, $V_{tho} \approx 0.3$ V, *DIBL* ≈100 mV/V, $V_D = 0.8$ V, $V_G = 0.5$, 0.8, and 1.0 V, and $T = 300$ K [16]; (iv) $L = 15$ nm, $V_{tho} \approx 0.2$ V, *DIBL* ≈120 mV/V, $V_D = 0.7$ V, $V_G = 0.7$ V, and $T = 300$ K [17]; and (v) $L = 15$ nm, $V_{tho} \approx 0.3$ V, *DIBL* ≈ 77 mV/V, $V_D = 0.7$ V, $V_G = 0.7$ V, and $T = 300$ K [18]. The above key parameters are also listed in Table 3-1. With all these key parameters, a scatter plot can be created as shown in Figure 3-4 in terms of the experimental and simulated ℓ versus the quantity of the functional expression $LV_D^{0.25}(V_G\text{-}V_{th})^{-0.5}(k_BT/q)^{0.5}(k_BT/qV_D)^{0.5}$. Apparently, all data seem to fall on or around a straight line. The slope of this line furnishes η with a value of $4.1V^{-0.25}$. Still, η remains constant, regardless of the channel length, gate and drain voltage, and temperature.

Section 3.4 Temperature Power Exponent Clarification

Some remarks can now be made to clarify the confusing α values in the open literature [3]-[8]. First of all, it is noticed that in case of bulk n-MOSFET two different values of α were produced: one of 0.5 [5], [7] and one of 0.75 [3]. This difference can be attributed to the different subband treatments during the parameter extraction process: Schrödinger-Poisson equations are numerically solved in [5], [7] whereas in [3] this was done by a triangular potential approximation [20]. Therefore, different subband levels can lead to different average thermal injection velocities, which in turn give rise to different ℓ values. Secondly, according to (22) a temperature range of 233 to 298 *K* in case of 55-nm bulk device [5], [7] is not large enough to affect the calculated $\tilde{L}$. In other words, $\tilde{L}$ is considerably insensitive to such a narrow temperature range. Consequently, the resulting apparent temperature power exponent was limited to 0.5 as reported in the previous work [4], [5]. Indeed, with the known η as input, fairly good reproduction can be achieved as depicted in Figure 3-4, without adjusting any parameters. The same interpretations also apply to

the $\alpha \approx 0.57$ case [6]: since the room temperature of operation was involved alone, the temperature effect of $\tilde{L}$ can no longer be examined. Only in a wide temperature range as done in the comprehensive study of [8], [19] can the linear relationship of $\ell \propto T$ as shown in Figure 3-4 actually occur. Thus, from the aspect of temperature dependencies, excellent coincidence with the data as shown in Figure 3-4 stresses that the existing backscattering coefficient extraction method [4] is valid.

Section 3.5 Results

This new compact k_BT-layer's width model, which links the width of thermal energy k_BT layer to the geometrical and bias parameters of the devices, is physically derived on the basis of a parabolic potential profile around the source-channel junction barrier of nanoscale-MOSFETs. Moreover, this proposed model is supported not only by experimental data, but also by various simulation works presented in the open literature. Only one fitting parameter remains constant in a wide range of channel length (10 to 65 nm), gate voltage (0.4 to 1.2 V), drain voltage (0.2 to 1.2 V), and temperature (100 to 500 K), which means that the capability of this compact model is universal.

Chapter 4

Re-examination of Mean-Free-path for Backscattering

When applying (1) to nanoscale MOSFETs to predict relevant current-voltage characteristic, we need to quantify the key backscattering coefficient r_c. However, there are two important parameters needed in r_c calculation. We have discussed the ℓ on the basis of a parabolic potential profile around the source-channel junction barrier and obtained a compact model of ℓ with the channel length, gate overdrive, drain voltage and temperature as input parameters. On the other hand, another parameter λ_0 has not been discussed yet. In Section 2.2.3, we extracted this information under near-equilibrium low field condition. When comparing (10) to compare with Monte Carlo results, it seems to have some differences between calculated and simulated r_c in the linear potential profile. In parabolic case, Figure 2-6 shows good agreement between calculation and simulation results. In this chapter, we will discuss the near-equilibrium mean-free-path for backscattering.

Section 4.1 Apparent Mean-Free-Path

At the end of Chapter 2, we pointed out that in the citation [12], the Monte Carlo simulations at room temperature in case of non-degenerate statistics on a linear channel potential profile have exhibited certain relationship: $\lambda' = \lambda_0 / \gamma$ with γ=1.5 to 2.0. Here λ' is the apparent mean-free-path that constitutes the following expression in the high field case:

$$r_c = \frac{\ell}{\ell + \lambda'} \tag{24}$$

Thus, some clarifications are demanded.

In order to achieve this goal, we perform Monte Carlo particle-based simulation on a silicon bulk conductor like what we have done in Chapter 2, but pay more attention on the velocity distribution on the top of the barrier and flux ration at the end of the k_BT layer.

Section 4.1.1 Mean-Free-Path Extraction in Linear Potential

First of all, we extract the mean free path from the simulated r_c using (25), instead of (10):

$$r_c = \frac{1-\exp(-L/\ell)}{\frac{\lambda'}{\ell}+1-\exp(-L/\ell)} \tag{25}$$

We denote the apparent mean free path as λ'. The validity of (25) has been proven in Chapter 2. By substituting the simulated r_c into (25), the underlying λ' can be obtained as depicted in Figure 4-1 versus applied voltage. From Figure 4-1, we can see that: (i) λ' falls below λ_0, and decreases with increasing applied voltage, leading to $\lambda' = \lambda_0/\gamma$ with γ = 1.5 to 2.5; and (ii) on average, λ' decreases with decreasing conductor length. However, it is supposed that the upper limit of λ_0 can be recovered only with increasing conductor length or decreasing applied voltage. On the other hand, the ratio of λ' to λ_0 appears to be a weak function of the lattice temperature. The same argument has been produced by the recent Monte Carlo simulations [12] devoted to a linear potential profile at lattice temperature of 300 K as we mentioned at the end of Chapter 2.

Section 4.1.2 Mean-Free-Path Extraction in Parabolic Potential

For a parabolic potential profile, the corresponding simulated r_c is displayed in Figure. 2-6. Here, the lines are calculated from (25) with λ' of 56, 105, and 155 nm for 300, 200, and 150 K, respectively. Good reproduction of the data for different conductor lengths, different temperatures, and, especially, different applied voltages can be gotten. Moreover, the reproduction can all be achieved with simply $\lambda' = \lambda_0$, without adjusting any parameters. This means no matter how the quasi-ballistic transport prevails in the k_BT layer ($\lambda' > \ell$), the quasi-equilibrium conditions still govern the backscattered carriers.

Section 4.2 Evidence for Carrier Heating

In Section 4.1, we see that the discrepancy in the mean-free-path in linear potential profile. This inconsistency can be contributed to the presence of the carrier heating. In citation [10], all the derivations are carried on the basis of the "relaxation length" approximation, which means that the mean-free-path is a constant, and is independent of the carrier energy or carrier temperature. However, as carriers transport under applied electric field, their energy should be changed, especially in the linear potential profile. Because of the lack of weak field regime near the injection point, the carriers experience a larger electric field in the linear one, and thus the deviation between the lattice temperature and carrier temperature would be possible. On the other hand, for a parabolic potential profile, as showing Figure 2-2, there is significant fraction of the k_BT layer, which can be determined as the weak field regime. Take this into consideration, although the deviations from the lattice temperature would be possible as entering into the remainder, the overall carrier heating in the k_BT layer should be weakened. Consequently, when the carriers are injected into the channel at the beginning of the k_BT layer, they immediately undergo the strong acceleration. Also, owing to the quasi-ballistic transport, the carrier temperature is expected to be higher than the lattice temperature and the

mean-free-path is therefore no longer independent of the carrier energy.

Section 4.2.1 Velocity Distribution at the Injection point

Concerning the difference between the lattice temperature and carrier temperature, the carrier velocity at the injection point is helpful as demonstrated in Figure 4-2 and 4-3. Figure 4-2 shows the velocity distribution of L=25nm at V_a=0.8 V and 300 K for two potential profiles. Figure 4-2 clearly shows that two significant differences between the potential profiles. First, the injected single hemi-Maxwellian velocity distribution is retained in the positively-directed carriers with the parabolic one, but it is split into two distinct components in the linear one: One of the longitudinal effective mass and one of the transverse effective mass. Second, the distribution of the negatively-directed or backscattered carriers appears to be wider in the linear potential profile than the parabolic one. The same result can be seen in Figure 4-3 for L=50nm at V_a=1.0 V and 150 K. This is evidence of carrier heating.

Section 4.2.2 Flux Ratio at the End of k_BT Layer

Carrier heating evidence also can be found at the end of k_BT layer ($x = \ell$). First of all, we replace x with ℓ in (9), leading to

$$b(0) = \frac{1 - e^{-1}}{\frac{\lambda_0}{\ell} + 1 - e^{-1}} a(0) + \frac{1}{(1 + \frac{\ell}{\lambda_0})e^{1} - \frac{\ell}{\lambda_0}} b(\ell) \qquad (26)$$

where $a(0)$ and $b(0)$ represent the incident and reflected flux at the origin, respectively, and $b(\ell)$ is the negatively-directed flux at the end of the k_BT layer. (26) also can be cited in the literature [10], which was derived on the basis of a Maxwillien shape distribution in both the forward and backward directions with in the context of the relaxation length approximation. In order to get the ratio of negatively-directed flux to positively-directed flux, we substitute (10) into (26) for $r_c = a(0)/b(0)$. Then,

accounting for the conservation of the current, the ratio $b(\ell)/a(\ell)$ can be straightforwardly calculated. Monte Carlo simulation program can provide the velocity distribution at the end of the k_BT layer. For example, Figure 4-4 shows velocity distribution of L=50 nm, T=200 K, and V_a=0.2 V at $x=\ell$. The velocity distribution also is split into two components, and velocity distribution of backscattered carrier is wider. The $b(\ell)/a(\ell)$ is the ratio of deep grey area to light grey area, like what we did to determine r_c at the injection point in Section 2.2.2. The calculated lines from (26) are shown in Figure 4-4 for linear potential profile. Also plotted in the figure are those of the Monte Carlo simulation. However, the calculated values are seen to fall below the simulation ones. This reveals the fact that the reflected flux at the end of k_BT layer can be enhanced in the presence of carrier heating. Only with decreasing applied voltage can the deviation between the simulation and model calculation be shortened.

Section 4.3 Results

We executed Monte Carlo simulations on a silicon bulk conductor to re-examine the channel backscattering theory in bulk nano-MOSFETs. Through these simulations, some important points can be addressed again:

(i) The near-equilibrium mean-free-path for backscattering λ_0, is independent of the potential profile.

(ii) λ' in a linear potential profile is lower than λ_0 of parabolic one due to the presence of the carrier heating. Evidence is highlighted by both the velocity distribution at the injection point and the flux ratio at the end of the k_BT layer.

Chapter 5

Conclusion

The backscattering coefficient is derived through the scattering matrix approach and verified by Monte Carlo simulations. Two important parameters, λ_0 and ℓ, constituting the channel backscattering coefficient have been taken into account. A parabolic barrier oriented compact model has been physically derived for ℓ. The validity of this compact model has been corroborated experimentally and by Monte Carlo simulation results. As for λ_0, the carrier heating as the origin of reduced mean-free-path is inferred on the basis of the simulated carrier velocity distribution at the injection point. Strikingly, for the parabolic potential case, the mean-free-paths remain consistent: $\lambda' = \lambda_o$. This indicates the absence or weakening of the carrier heating in the layer of interest, valid only for a parabolic potential barrier

References

[1] M. S. Lundstrom, "Elementary scattering theory of the Si MOSFET," *IEEE Electron Device Letters*, vol. 18, pp. 361-363, July 1997.

[2] M. S. Lundstrom and Z. Ren, "Essential physics of carrier transport in nanoscale MOSFETs," *IEEE Trans. Electron Devices*, vol. 49, pp. 133-141, Jan. 2002.

[3] M.-J. Chen, H.-T. Huang, Y.-C. Chou, R.-T. Chen, Y.-T. Tseng, P.-N. Chen, and C. H. Diaz, "Separation of channel backscattering coefficients in nanoscale MOSFETs," *IEEE Trans. Electron Devices*, vol. 51, pp. 1409-1415, Sept. 2004.

[4] M.-J. Chen, H.-T. Huang, K.-C. Huang, P.-N. Chen, C.-S. Chang, and C. H. Diaz, "Temperature dependent channel backscattering coefficients in nanoscale MOSFETs," in *IEDM Tech. Dig.*, pp. 39-42, Dec. 2002.

[5] M. J. Chen, S. G. Yan, R. T. Chen, C. Y. Hsieh, P. W. Huang, and H. P. Chen, "Temperature-oriented experiment and simulation as corroborating evidence of MOSFET backscattering theory," *IEEE Electron Device Lett.*, vol. 28, pp.177-179, Feb. 2007.

[6] A. Rahman and M. S. Lundstrom, "A compact scattering model for the nanoscale double-gate MOSFET," *IEEE Trans. Electron Devices*, vol. 49, pp. 481-489, March 2002.

[7] M. J. Chen, R. T. Chen, and Y. S. Lin, "Decoupling channel backscattering coefficients in nanoscale MOSFETs to establish near-source channel conduction-band profiles," in *Silicon Nanoelectronics Workshop*, pp. 50-51, June 2005.

[8] P. Palestri, D. Esseni, S. Eminente, C. Fiegna, E. Sangiorgi, and L. Selmi,

" Understanding quasi-ballistic transport in nano-MOSFETs : Part I – Scattering in the channel and in the drain," *IEEE Trans. Electron Devices*, vol. 52, pp. 2727-2735, Dec. 2005.

[9] Mark Lundstrom, *Fundamentals of Carrier Transport, second edition*, School of Electrical and Computer Engineering Purdue University, West Lafayette, Indiana, USA: Cambridge University Press, 2000.

[10] R. Clerc, P. Palestri, and L. Selmi, "On the physical understanding of the kT-layer concept in quasi-ballistic regime of transport in nanoscale devices," *IEEE Trans. Electron Devices*, vol. 53, pp. 1634-1640, July 2006.

[11] S. Datta, *Electronic Transport in Mesoscopic System*, Cambridge, U.K.: Cambridge Univ. Press, 1995.

[12] P. Palestri R. Clerc, and D. Esseni, L. Lucci, and L. Selmi, "Multi-subband-Monte-Carlo investigation of the mean free path and of the kT layer in degenerated quasi ballistic nanoMOSFETs," in *IEDM Tech. Dig.*, , pp.945-948, Dec. 2006.

[13] http://www.nanohub.org

[14] M. J. Chen and L. F. Lu, "A parabolic potential barrier oriented compact model for the kBT-layer's width in nano-MOSFETs," *IEEE Trans. Electron Devices*, vol. 53, pp. 1265-1268, May 2008.

[15] R. Clerc, P. Palestri, and L. Selmi, "On the physical understanding of the kT-layer concept in quasi-ballistic regime of transport in nanoscale devices," *IEEE Trans. Electron Devices*, vol. 53, pp. 1634-1640, July 2006.

[16] E. Fuchs, P. Dollfus, G. L. Carval, S. Barraud, D. Villanueva, F. Salvetti, H. Jaouen, and T. Skotnicki, " A new backscattering model giving a description of the quasi-ballistic transport in nano-MOSFET," *IEEE Trans. Electron Devices*, vol. 52, pp. 2280-2289, Oct. 2005.

[17] J. Saint-Martin, A. Bournel, and P. Dollfus, "On the ballistic transport in nanometer-scaled DG MOSFETs," *IEEE Trans. Electron Devices*, vol. 51, pp. 1148-1155, July 2004.

[18] D. Querlioz, J. Saint-Martin, K. Huet, A. Bournel, V. Aubry-Fortuna, C. Chassat, S. Galdin-Retailleau, and P. Dollfus, "On the ability of the particle Monte Carlo technique to include quantum effects in nano-MOSFET simulation," *IEEE Trans. Electron Devices*, vol. 54, pp. 2232-2242, Sept. 2007.

[19] S. Eminente, D. Esseni, P. Palestri, C. Fiegna, L. Selmi and E. Sangiorgi,, " Understanding quasi-ballistic transport in nano-MOSFETs : Part II – Technology scaling along the IRTS," *IEEE Trans. Electron Devices*, vol. 52, pp. 2736-2743, Dec. 2005.

[20] K. N. Yang, H. T. Huang, M. C. Chang, C. M. Chu, Y. S. Chen, M. J. Chen, Y. M. Lin, M. C. Yu, S. M. Jang, C. H. Yu, and M. S. Liang, "A physical model for hole direct tunneling current in p^+ poly-gate pMOSFETs with ultrathin gate oxides," *IEEE Trans. Electron Devices*, vol. 47, pp. 2161–2166, Nov. 2000.

	L (nm)	Vtho (V)	DIBL (mV/V)	V_D (V)	V_G (V)	T (K)
M. S. Lundstrom, et al. [2]	10	0.33	140	0.6	0.6	300
A. Rahman, et al. [6]	20	0.33	25	0.2	0.55	300
P. Palestri, et al. [8]	14~37	0.3	110	1	1	100~500
E. Fuchs, et al. [16]	25	0.3	100	0.8	0.5~1.0	300
J. Saint-Martin, et al. [17]	15	0.2	120	0.7	0.7	300
D. Querlioz, et al. [18]	15	0.3	77	0.7	0.7	300
S. Eminente, et al. [19]	14~65	0.3	11~230	1.0~1.2	1.0~1.2	300

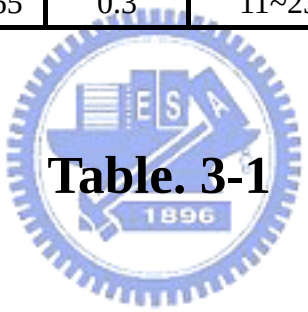

Table. 3-1

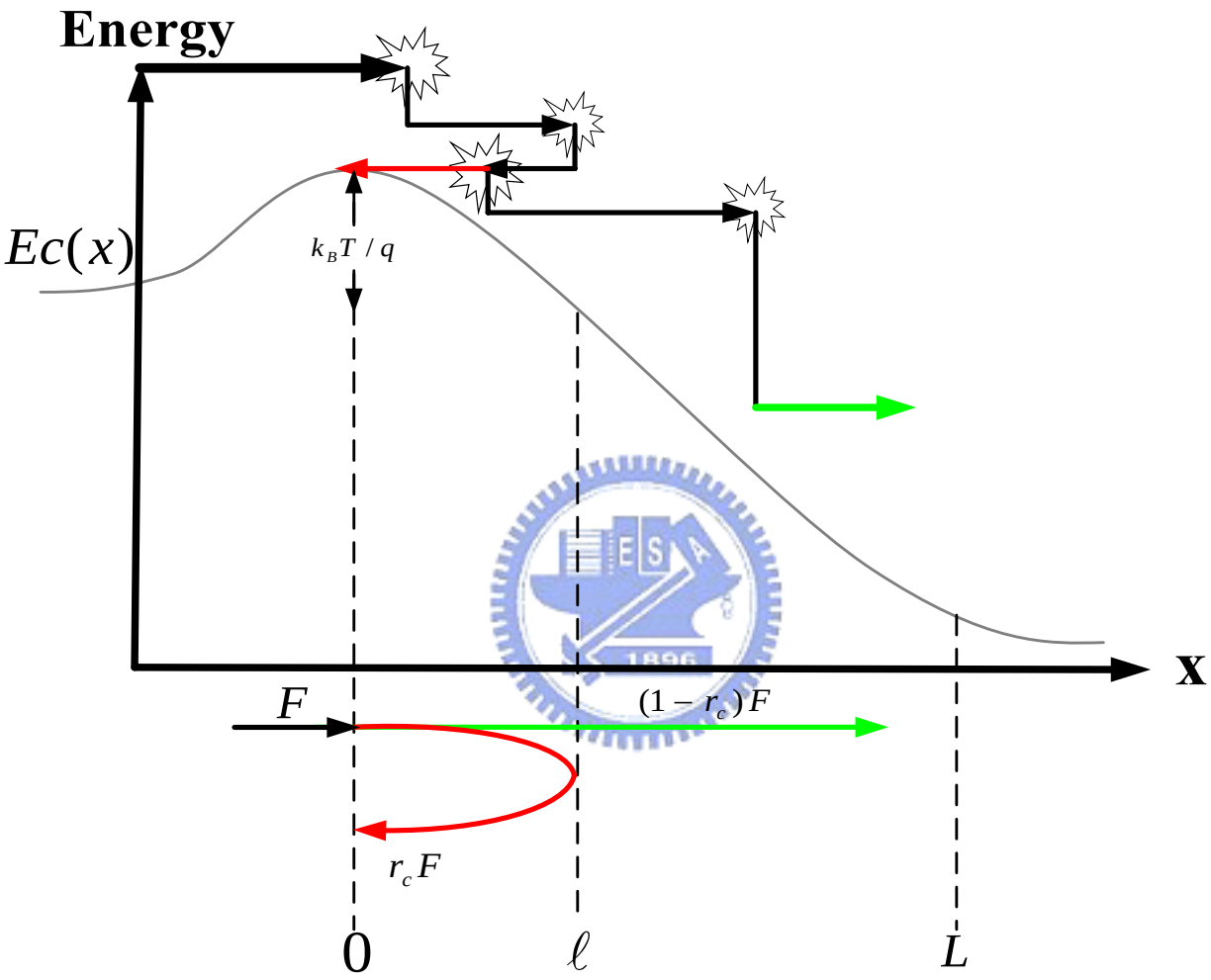

Fig.1-1

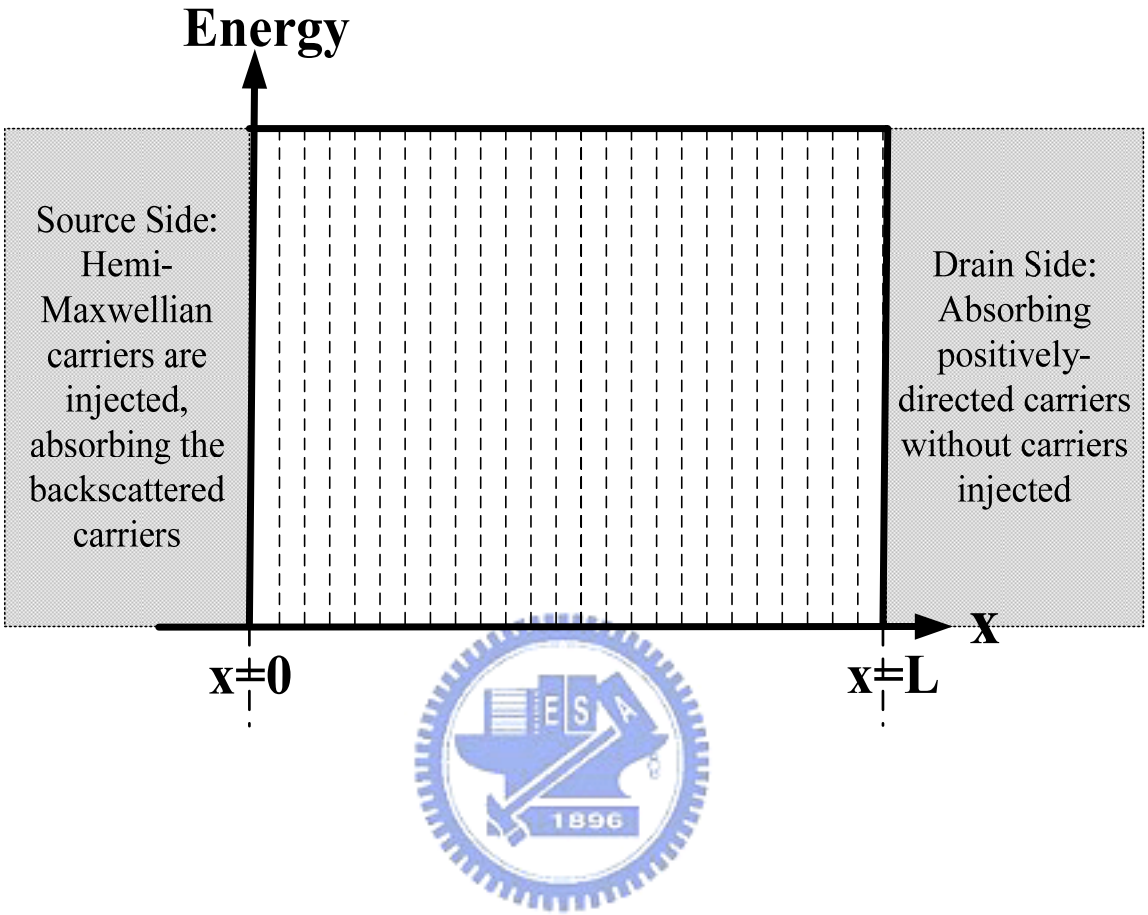
Energy
Source Side: Hemi-Maxwellian carriers are injected, absorbing the backscattered carriers
Drain Side: Absorbing positively-directed carriers without carriers injected
x
x=0
x=L

Fig.2-1

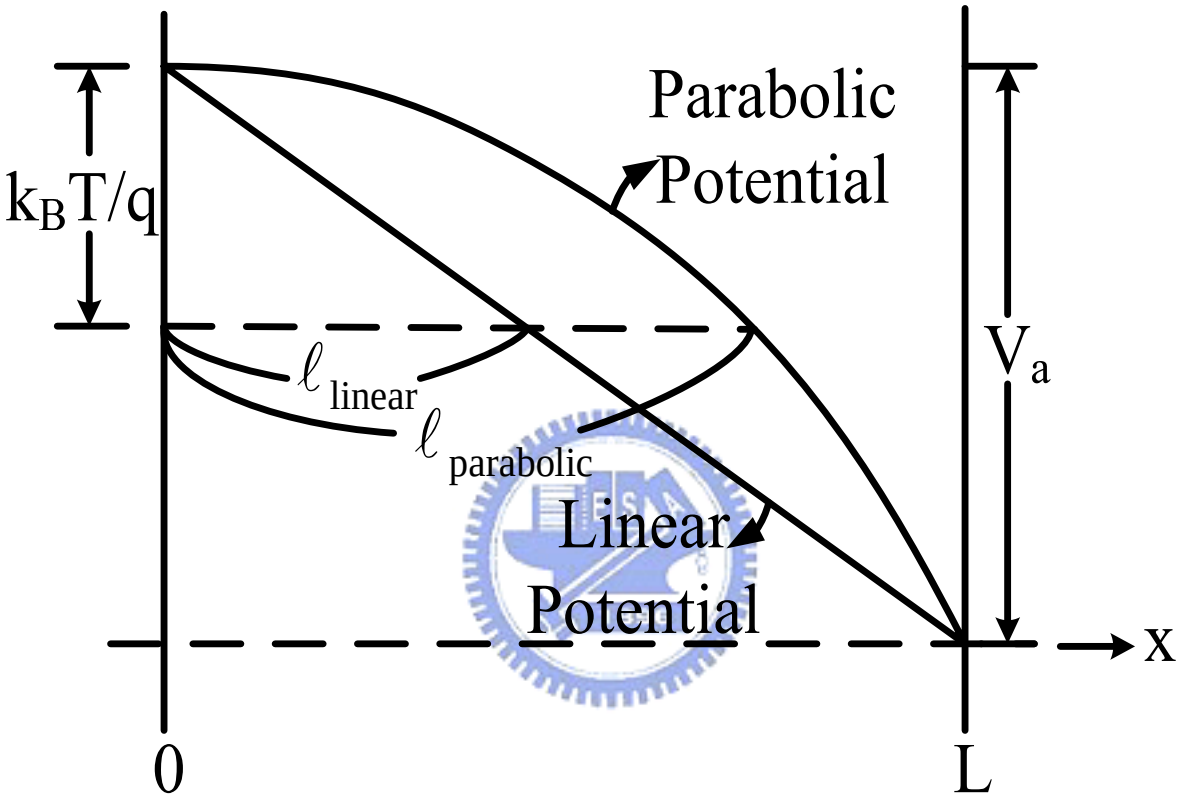
Parabolic
Potential
k_BT/q
V_a
ℓ_{linear}
$\ell_{parabolic}$
Linear
Potential
x
0
L

Fig.2-2

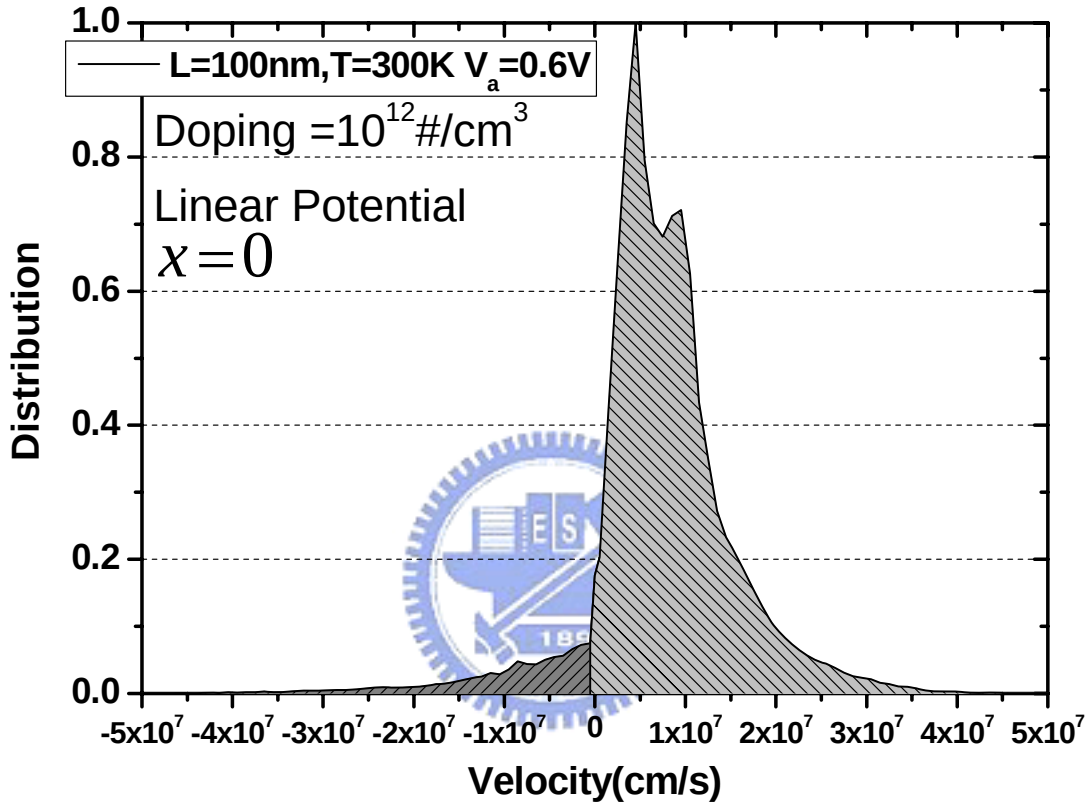
L=100nm,T=300K V_a=0.6V
Doping =10^12#/cm^3
Linear Potential
x=0
Distribution
Velocity(cm/s)
1.0
0.8
0.6
0.4
0.2
0.0
-5x10^7 -4x10^7 -3x10^7 -2x10^7 -1x10^7 0 1x10^7 2x10^7 3x10^7 4x10^7 5x10^7

Fig.2-3

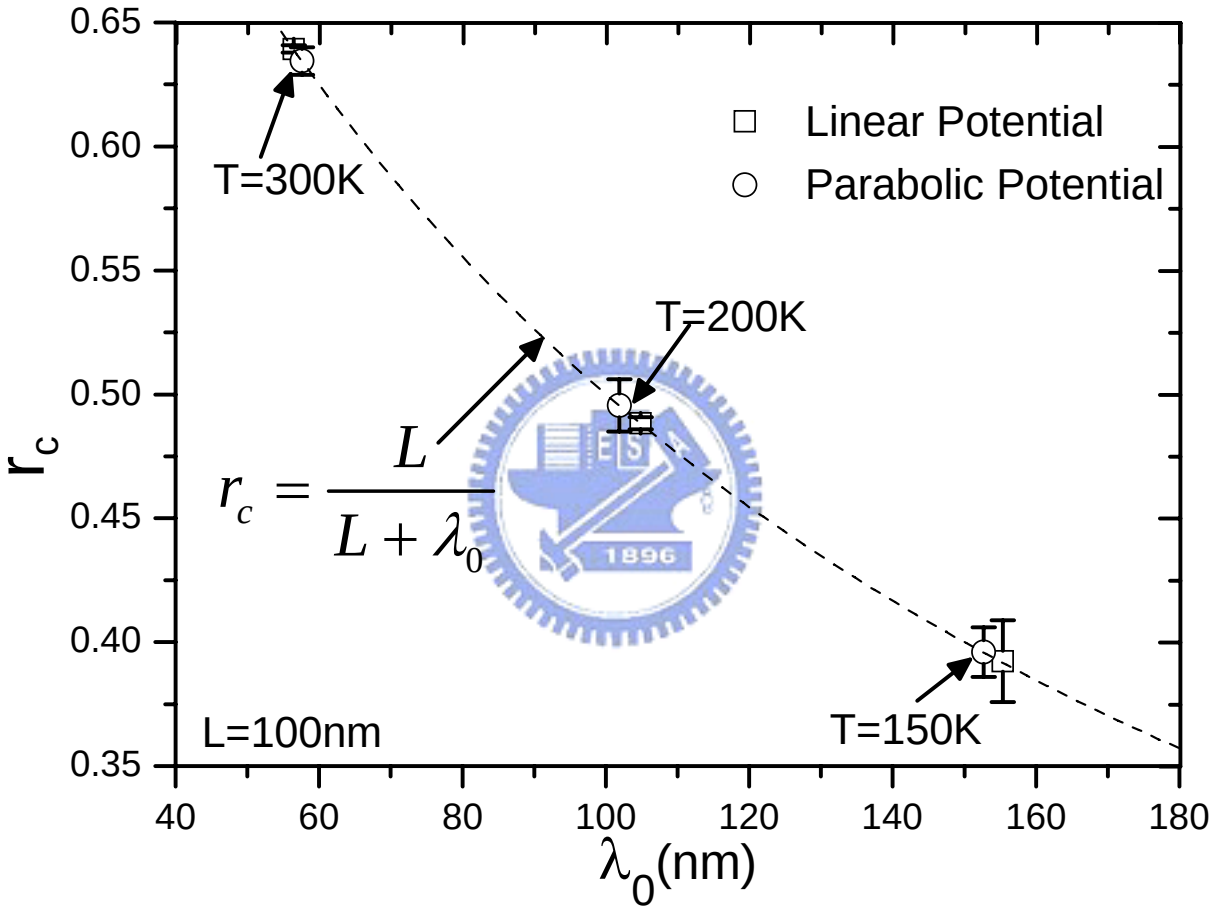
0.65
0.60
0.55
0.50
0.45
0.40
0.35
r_c
40
60
80
100
120
140
160
180
λ_0(nm)
□ Linear Potential
○ Parabolic Potential
T=300K
T=200K
T=150K
$r_c = \frac{L}{L + \lambda_0}$
L=100nm

Fig.2-4

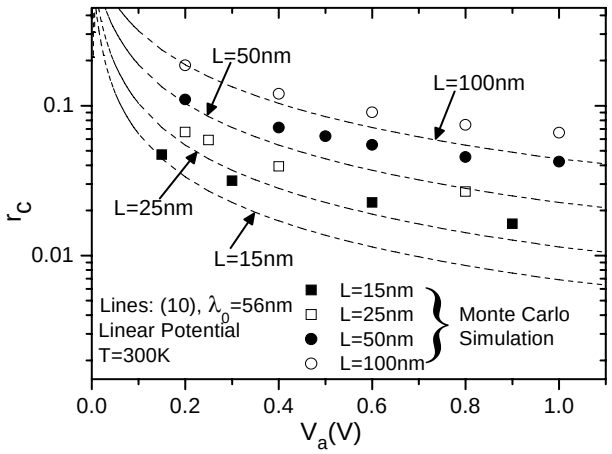
L=50nm
L=100nm
L=25nm
L=15nm
0.1
0.01
r_c
Lines: (10), λ_0=56nm
Linear Potential
T=300K
L=15nm
L=25nm
L=50nm
L=100nm
Monte Carlo
Simulation
0.0
0.2
0.4
0.6
0.8
1.0
V_a(V)

(a)

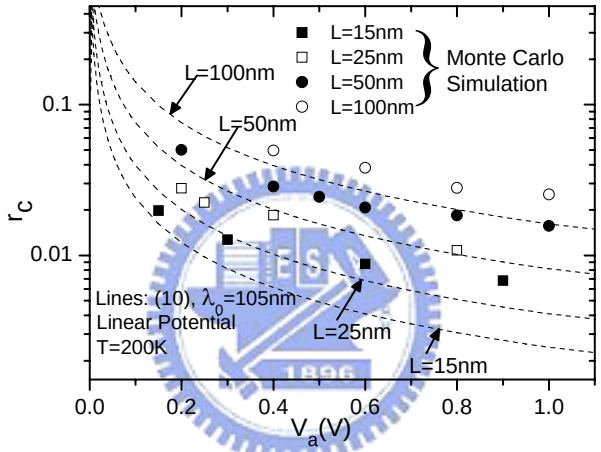
L=15nm
L=25nm
L=50nm
L=100nm
Monte Carlo
Simulation
L=100nm
L=50nm
0.1
0.01
r_c
Lines: (10), λ_0=105nm
Linear Potential
T=200K
L=25nm
L=15nm
0.0
0.2
0.4
0.6
0.8
1.0
V_a(V)

(b)

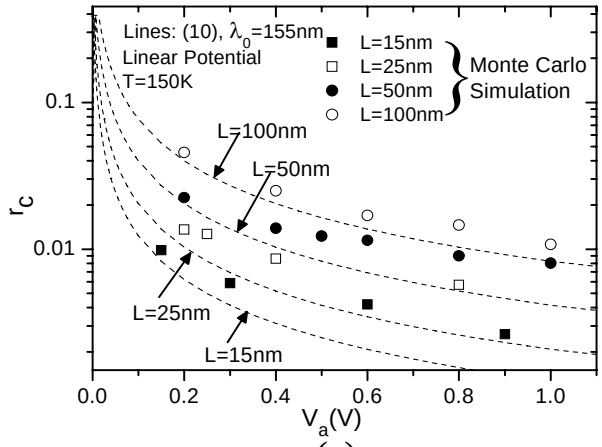
Lines: (10), λ_0=155nm
Linear Potential
T=150K
L=15nm
L=25nm
L=50nm
L=100nm
Monte Carlo
Simulation
L=100nm
L=50nm
0.1
0.01
r_c
L=25nm
L=15nm
0.0
0.2
0.4
0.6
0.8
1.0
V_a(V)

(c)

Fig.2-5

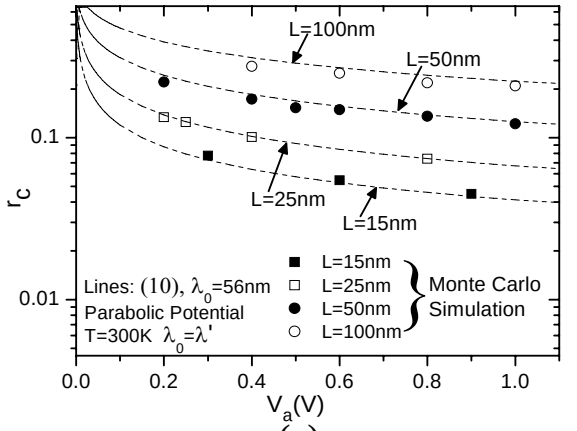
L=100nm
L=50nm
L=25nm
L=15nm
0.1
0.01
r_c
Lines: (10), λ_0=56nm
Parabolic Potential
T=300K $\lambda_0=\lambda'$
L=15nm
L=25nm
L=50nm
L=100nm
Monte Carlo Simulation
0.0
0.2
0.4
0.6
0.8
1.0
V_a(V)

(a)

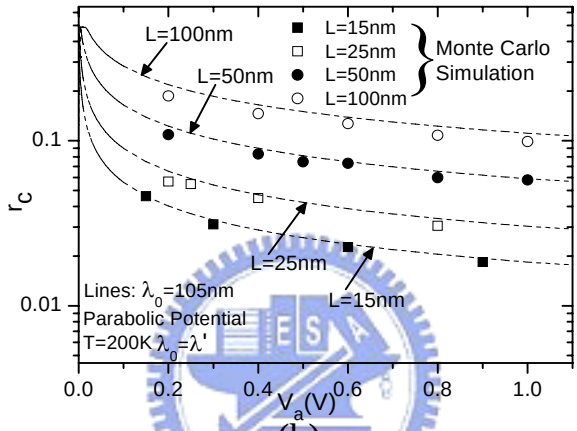
L=100nm
L=50nm
L=25nm
L=15nm
0.1
0.01
r_c
Lines: λ_0=105nm
Parabolic Potential
T=200K $\lambda_0=\lambda'$
L=15nm
L=25nm
L=50nm
L=100nm
Monte Carlo Simulation
0.0
0.2
0.4
0.6
0.8
1.0
V_a(V)

(b)

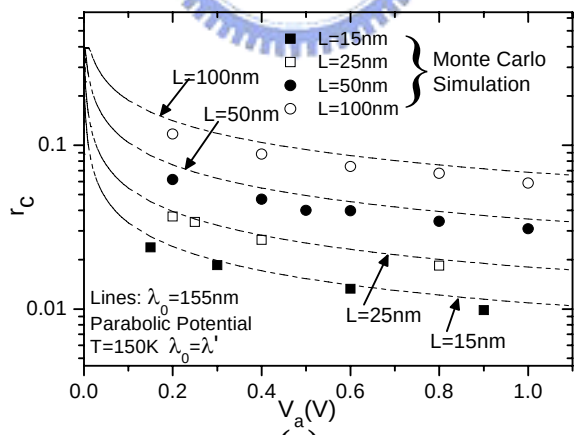
L=100nm
L=50nm
L=25nm
L=15nm
0.1
0.01
r_c
Lines: λ_0=155nm
Parabolic Potential
T=150K $\lambda_0=\lambda'$
L=15nm
L=25nm
L=50nm
L=100nm
Monte Carlo Simulation
0.0
0.2
0.4
0.6
0.8
1.0
V_a(V)

(c)

Fig.2-6

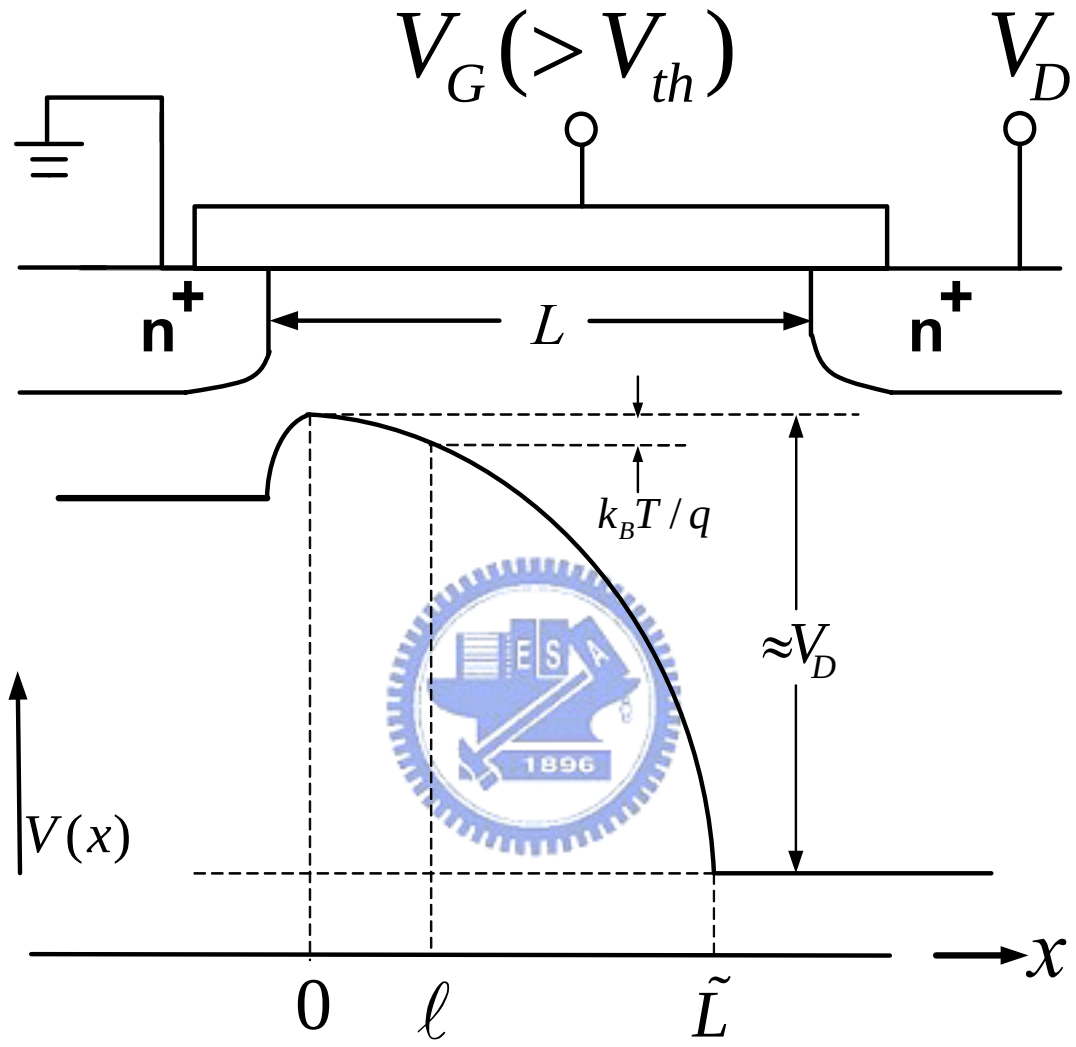

Fig. 3-1

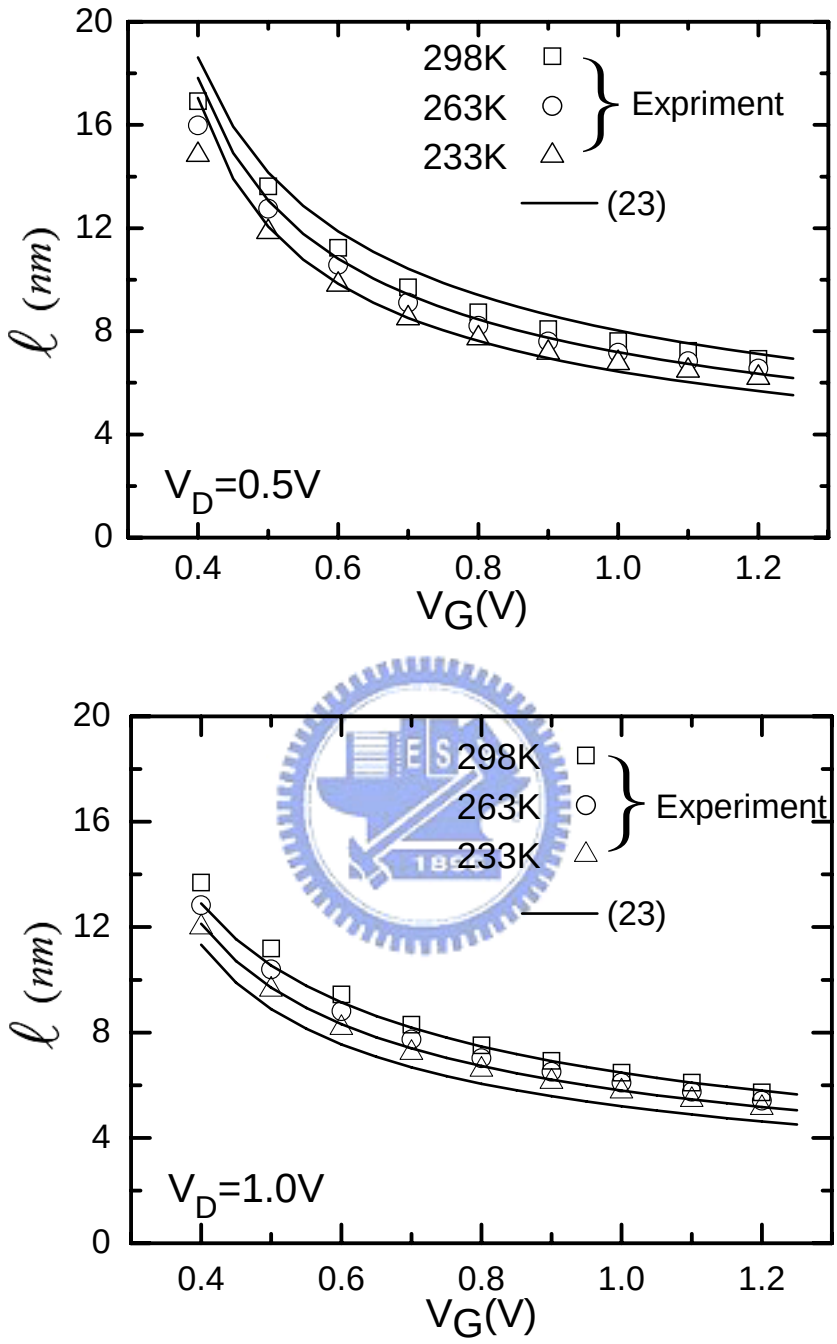
20
16
12
8
4
0
ℓ (nm)
298K
263K
233K
Expriment
(23)
V_D=0.5V
0.4
0.6
0.8
1.0
1.2
V_G(V)
20
16
12
8
4
0
ℓ (nm)
298K
263K
233K
Experiment
(23)
V_D=1.0V
0.4
0.6
0.8
1.0
1.2
V_G(V)

Fig.3-2

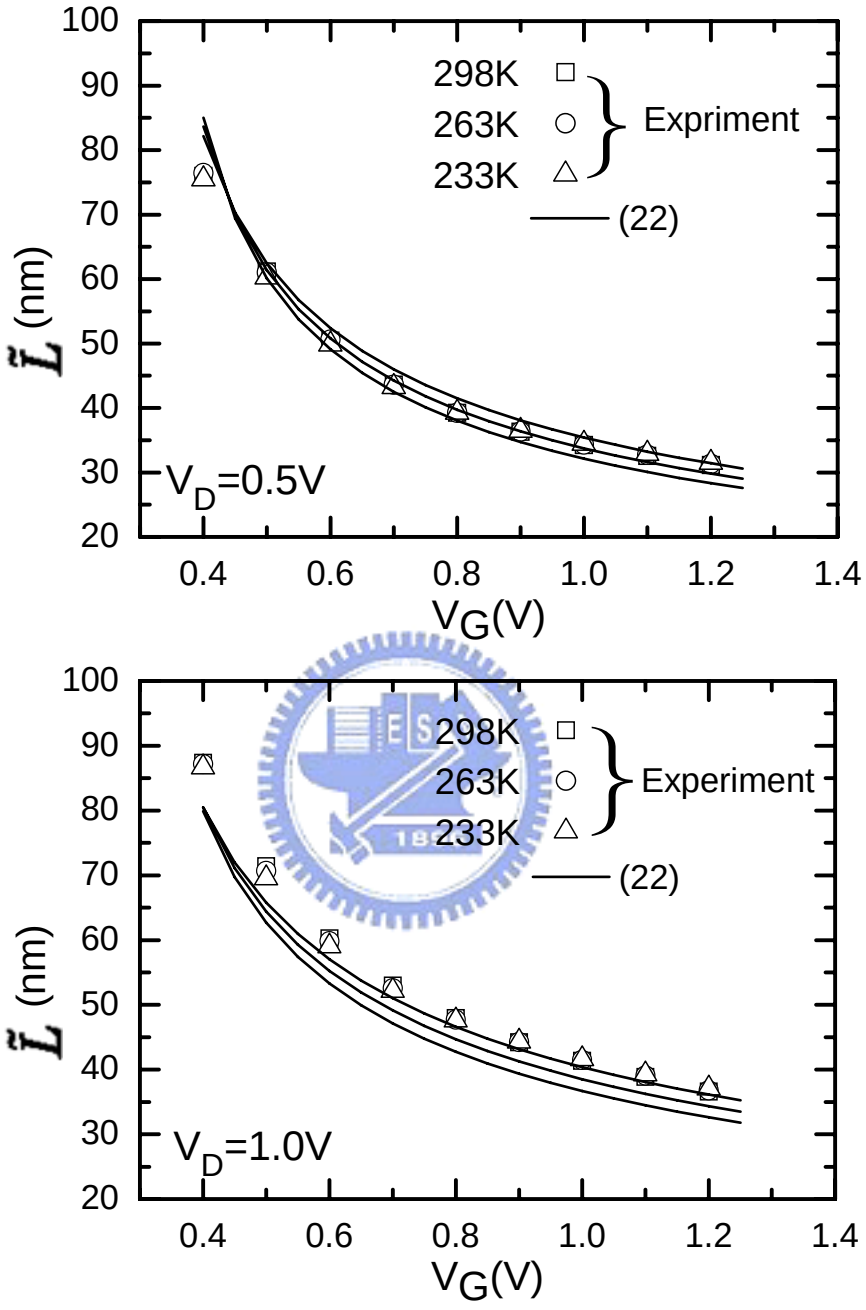
100
90
80
70
60
50
40
30
20
$\tilde{L}$ (nm)
298K
263K
233K
Expriment
(22)
V_D=0.5V
0.4
0.6
0.8
1.0
1.2
1.4
V_G(V)
100
90
80
70
60
50
40
30
20
$\tilde{L}$ (nm)
298K
263K
233K
Experiment
(22)
V_D=1.0V
0.4
0.6
0.8
1.0
1.2
1.4
V_G(V)

Fig.3-3

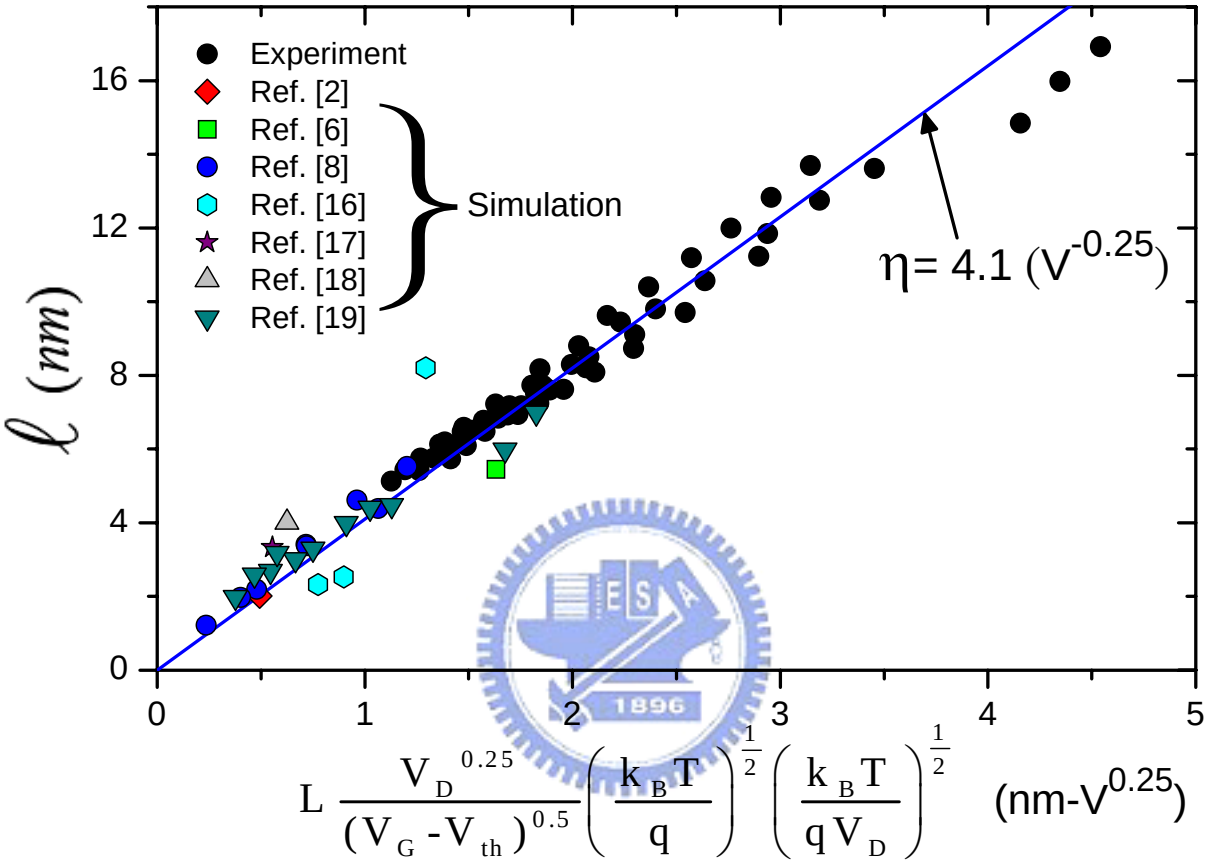
Experiment
Ref. [2]
Ref. [6]
Ref. [8]
Ref. [16]
Ref. [17]
Ref. [18]
Ref. [19]
Simulation
η= 4.1 (V-0.25)
ℓ (nm)
0
4
8
12
16
0
1
2
3
4
5
$L\frac{V_D^{0.25}}{(V_G - V_{th})^{0.5}}\left(\frac{k_B T}{q}\right)^{\frac{1}{2}}\left(\frac{k_B T}{q V_D}\right)^{\frac{1}{2}}$ (nm-V0.25)

Fig.3-4

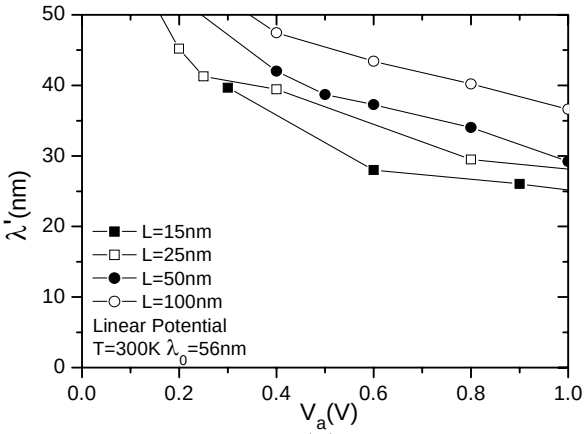
λ'(nm)
V_a(V)
L=15nm
L=25nm
L=50nm
L=100nm
Linear Potential
T=300K λ_0=56nm

(a)

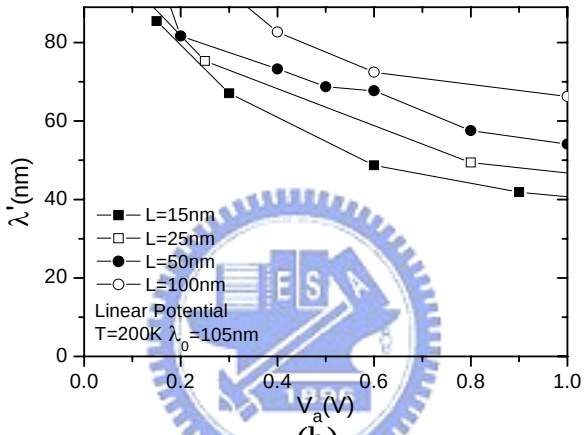
λ'(nm)
V_a(V)
L=15nm
L=25nm
L=50nm
L=100nm
Linear Potential
T=200K λ_0=105nm

(b)

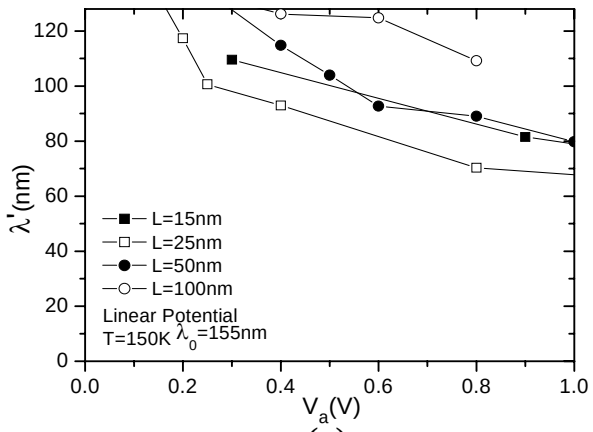
λ'(nm)
V_a(V)
L=15nm
L=25nm
L=50nm
L=100nm
Linear Potential
T=150K λ_0=155nm

(c)

Fig.4-1

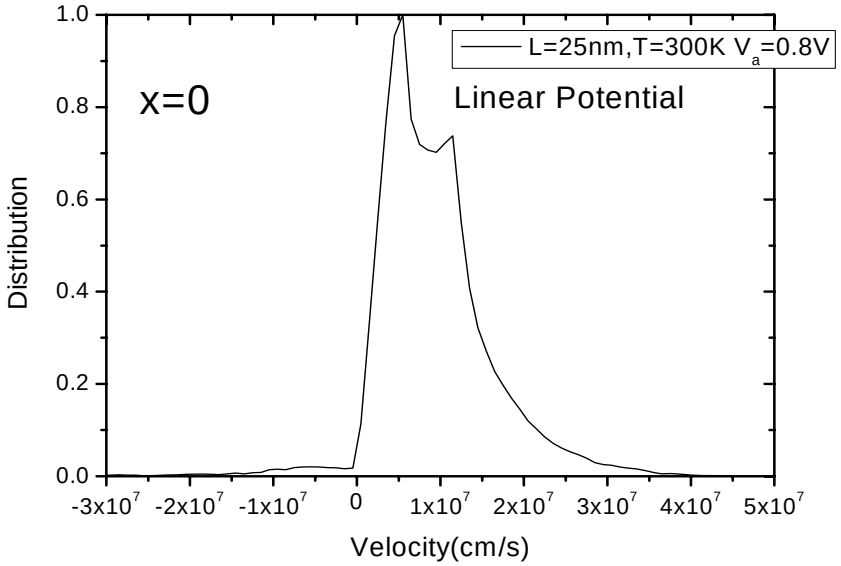
L=25nm,T=300K V_a=0.8V
x=0
Linear Potential
Distribution
Velocity(cm/s)

(a)

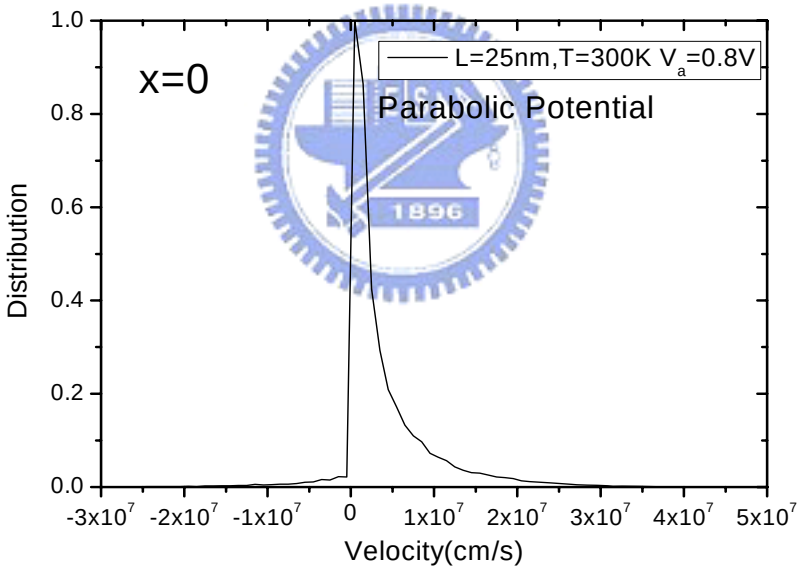
L=25nm,T=300K V_a=0.8V
x=0
Parabolic Potential
Distribution
Velocity(cm/s)

(b)

Fig.4-2

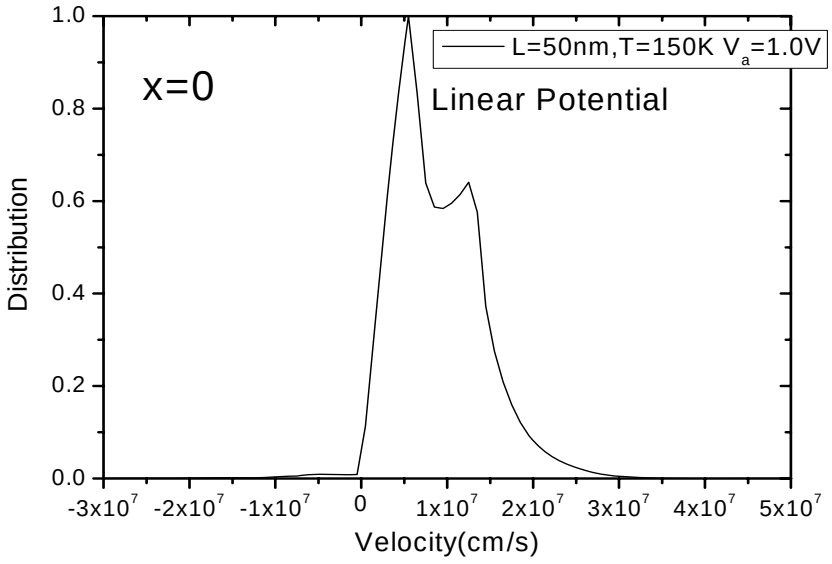
1.0
0.8
0.6
0.4
0.2
0.0
Distribution
x=0
L=50nm,T=150K V_a=1.0V
Linear Potential
-3x10^7
-2x10^7
-1x10^7
0
1x10^7
2x10^7
3x10^7
4x10^7
5x10^7
Velocity(cm/s)

(a)

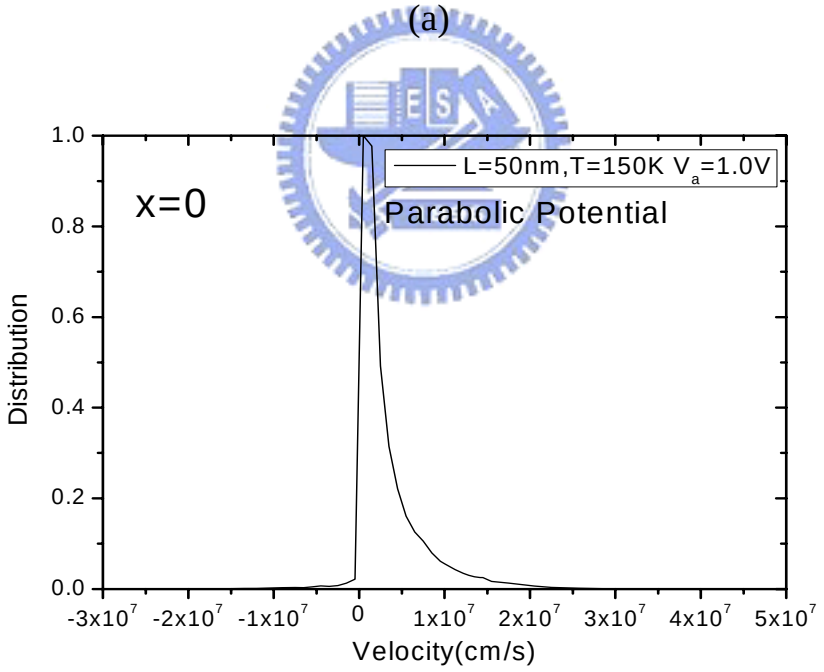
1.0
0.8
0.6
0.4
0.2
0.0
Distribution
x=0
L=50nm,T=150K V_a=1.0V
Parabolic Potential
-3x10^7
-2x10^7
-1x10^7
0
1x10^7
2x10^7
3x10^7
4x10^7
5x10^7
Velocity(cm/s)

(b)

Fig.4-3

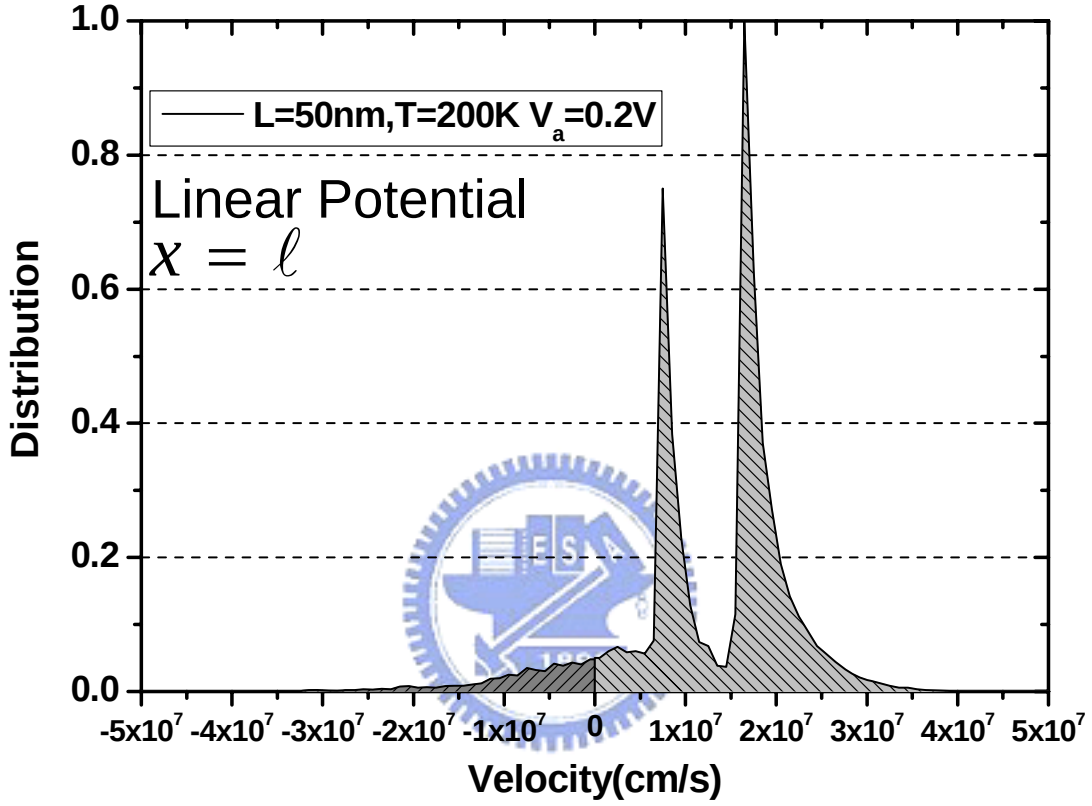
L=50nm,T=200K V_a=0.2V
Linear Potential
x = ℓ
Distribution
1.0
0.8
0.6
0.4
0.2
0.0
-5x10^7 -4x10^7 -3x10^7 -2x10^7 -1x10^7 0 1x10^7 2x10^7 3x10^7 4x10^7 5x10^7
Velocity(cm/s)

Fig.4-4

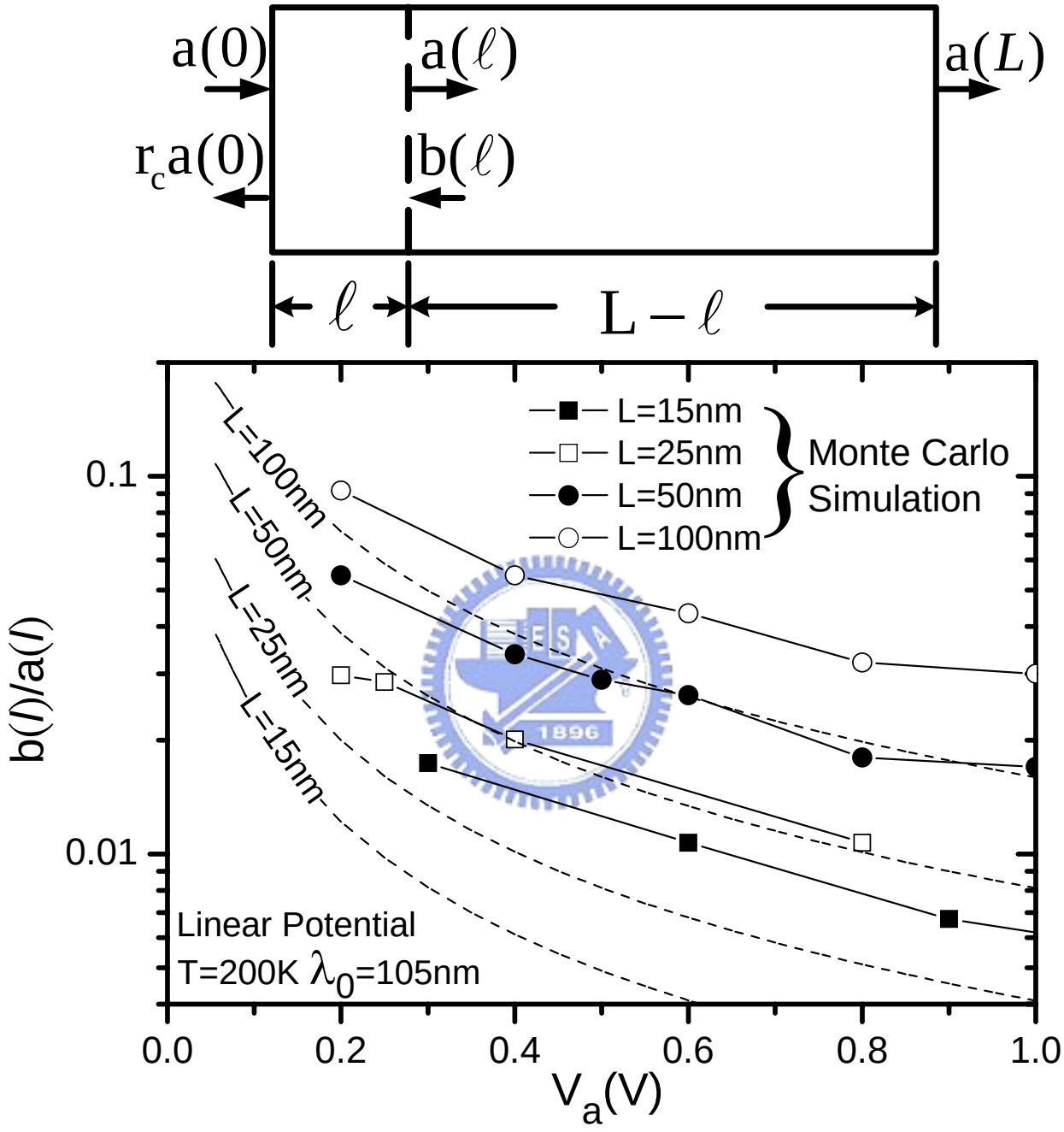
a(0)
a(ℓ)
a(L)
r_c a(0)
b(ℓ)
ℓ
L – ℓ
L=15nm
L=25nm
L=50nm
L=100nm
Monte Carlo Simulation
L=100nm
L=50nm
L=25nm
L=15nm
Linear Potential
T=200K λ0=105nm
b(l)/a(l)
0.1
0.01
0.0
0.2
0.4
0.6
0.8
1.0
Va(V)

Fig.4-5